

Special Section on EG VCBM 2024

Analyzing the effect of undermining on suture forces during simulated skin flap surgeries with a three-dimensional finite element method



Wenzhangzhi Guo ^{a,b,c,*}, Allison Tsz Kwan Lau ^{a,b}, Joel C. Davies ^d, Vito Forte ^{c,e}, Eitan Grinspun ^b, Lueder Alexander Kahrs ^{a,b,e,f,g}

^a Medical Computer Vision and Robotics Lab, University of Toronto, Toronto, Ontario, Canada

^b Department of Computer Science, University of Toronto, 40 St George St, Toronto, M5S 2E4, Canada

^c Wilfred and Joyce Postlum Centre for Image Guided Innovation and Therapeutic Intervention, The Hospital for Sick Children, 170 Elizabeth St, Toronto, M5G 1E8, Canada

^d Department of Otolaryngology - Head and Neck Surgery, Sinai Health System, University of Toronto, 600 University Ave, Toronto, M5G 1X5, Canada

^e Department of Otolaryngology - Head and Neck Surgery, University of Toronto, 600 University Ave, Toronto, M5G 1X5, Canada

^f Department of Mathematical and Computational Sciences, University of Toronto Mississauga, 3359 Mississauga Rd, Mississauga, L5L 1C6, Canada

^g Institute of Biomedical Engineering, University of Toronto, 164 College St, Toronto, M5S 3G9, Canada

ARTICLE INFO

Keywords:
Simulation
Visualization
Force analysis

ABSTRACT

Skin flaps are common procedures used by surgeons to cover an excised area during the reconstruction of a defect. It is often a challenging task for a surgeon to come up with the most optimal design for a patient. In this paper, we set up a simulation system based on the finite element method for one of the most common flap types — the rhomboid flap. Instead of using the standard 2D planar patch, we constructed a 3D patch with multiple layers. This allowed us to investigate the impact of different undermining areas and depths. We compared the suture forces for each case and identified vertices with the largest suture force. The shape of the final suture line is also visualized for each case, which is an important clue when deciding on the most optimal skin flap orientation according to medical textbooks. We found that under the optimal undermining setup, the maximum suture force is around 0.7 N for top of the undermined layer and 1.0 N for bottom of the undermined layer. When measuring difference in final suture line shape, the maximum normalized Hausdorff distance is 0.099, which suggests that different undermining region can have significant impact on the shape of the suture line, especially in the tail region. After analyzing the suture force plots, we provided recommendations on the most optimal undermining region for rhomboid flaps.

1. Introduction

Skin flaps are commonly used in reconstructive surgeries following resection of cutaneous lesions [1]. The optimal skin flap design for each patient depends on many factors including nearby facial structures, aesthetic sub-unit(s), skin laxity, and the size/shape of the lesion. It often takes years of training for a surgeon to create an optimal design for a patient based on the factors described. To assist surgeons in making such decisions, simulation techniques are often used. These simulations can provide invaluable insights as well as provide visualizations to assist surgeons in making more informed decisions. One historical challenge in the use of simulations in clinical practice is the lack of objective data to drive clinical practice. For example, determining the optimal degree of skin undermining following resection of a cutaneous

lesion to minimize tension along relaxed skin tension lines (RSTLs) and limit the impact on movement of adjacent tissue in nearby anatomic subunits can be challenging. This information could assist surgeons in flap design early in the process of planning out local resections and reconstructions. In this paper, we focus on setting up a finite element method (FEM) simulation for a 3D mesh of a rhomboid flap. Previously, the suture forces of a 2D rhomboid flap was investigated [2]. We hypothesized that additional insights can be obtained if the skin patch is simulated with a 3D mesh. Using 3D simulation has several advantages over the traditional 2D models. One significant benefit is the ability to accurately capture 3D deformation, allowing for a more realistic representation of tissue behavior during suturing. Also, 3D simulations enable studying complex interactions between the skin flap and underlying tissue layers, providing insights that may not be attainable with 2D models. The main contributions of the paper are:

* Correspondence to: 40 St George St, Toronto, ON M5S 2E4, Canada.

E-mail address: wenzhi.guo@mail.utoronto.ca (W. Guo).

- We designed a general pipeline for generating 3D meshes from 2D templates for skin flap simulations that can be used to analyze various skin flap types.
- We investigated the effect of varying the amount of undermining in a skin flap simulation in a systematic and quantitative way.
- We compared the suture force and final suture line of the simulation with different amount of undermining for rhomboid flaps. We also gave recommendations on the most optimal undermining areas based on our analysis.
- We created visualizations of skin flap procedures based on a patient's 3D face scan.

2. Related works

2.1. Soft tissue simulation

In order to create realistic simulation of different flap procedures, the accurate simulation of soft tissue and skin would be essential. Soft tissues are often modeled as hyperelastic solids and they exhibit different properties such as viscoelasticity and incompressibility [3]. Different models have been proposed to address the viscoelasticity of soft tissues, from the most widely used Standard Linear Solid (SLS) model [4] to more recent models such as the generalized Wiechert model [5], and double Maxwell-arm Wiechert representative model [6]. In order to avoid volume locking, the incompressibility property is usually addressed by introducing different constraints such as the 1-ring neighborhood [7] constraints and zonal volume constraints [8]. Specifically in Sheen et al.'s recent work [8], a new method was proposed to handle the incompressibility of soft tissue that allowed tissue deformation to be modeled more accurately under a FEM framework. In this work, the incompressibility property of soft tissue was addressed by the introduction of zonal volume constraints (to ensure the volume of each zone was preserved), while fine-scale deformations were controlled through local compression penalty terms (to ensure each element was not severely compressed). To improve accuracy in surgical guidance, Pereira et al. [9] modeled tissue retraction with eXtended Finite Element Method (XFEM) and the preoperative medical images can be updated with the displacement fields from the simulation to better visualize deformations.

2.2. Surgical simulators

There have been many surgical simulators built by different research groups and companies for educational purposes. Eftychios Sifakis' group has been focusing on developing interactive skin flap simulators for a while. One of their recent works is an interactive skin flap simulator that takes a 3D mesh of a head model as input and the user could construct various flaps with tools provided in the application [10]. To achieve interactive rate for the simulation, the application utilizes parallel computing on a GPU along with projective dynamics as the physics model. Various surgical operations were implemented such as skin incision, undermining, deep tissue cutting, excision, and suturing. Prior to this work, Sifakis' group also developed slightly different versions of the interactive skin flap simulator where they achieved the computational efficiency by using a front-end (e.g. visualization on a tablet) and a back-end (intensive computation on the server) structure with a novel framework for computational efficiency in their GRIDiron paper [11].

Table 1

Overview of pipeline and corresponding software packages used at each stage. The letter(s) after each pipeline stage represents corresponding stages in Fig. 1 and detailed steps with each software package can be seen in the corresponding video in the supplementary materials.

Pipeline stage	Software used
Flap design (a)	None
2D mesh generation (b)	Triangle [23,24]
Mesh extrusion (c)	Paraview [25] (video1)
3D mesh generation (d)	Blender [26] (video2) + GMsh [27] (video3)
Run simulation (e-f)	MATLAB [28] + Bartels [29]
Visualization (g-h)	MATLAB [28] + Blender [26]

2.3. Skin flap simulations

On the other hand, instead of aiming for interactivity, there are also various physics-based simulations created by several groups to visualize stress fields in commonly used skin flaps with pre-defined geometries. Most of these simulations are built based on commercial finite element method (FEM) software and the goal is to provide insights and visualizations of skin flaps based on stress/strain analysis. In [12–14], the authors introduced the basic setup of a FEM skin flap simulation framework, provided visualizations of stress fields, and made some qualitative analysis based on the stress field such as location of maximum tension in a particular flap. In [15], in addition to stress fields visualization, Copek et al. also provided comparison of in vivo model with the FEM result as a validation to their simulation. There are also some works that focus on different configurations of one flap type. In [16], Rajabi et al. analyzed von Mises stress, maximum compressive principal stress, and deformed configurations of different configurations of the rhomboid flap and proposed a modified flap geometry based on the findings. Similarly in [17], Remache et al. showed how closure force varied after the flap angle, material properties, and choices of corner stitches changed for V-Y shaped advancement flap.

In addition to flap configurations, there are also literatures that focus on modeling the effect of different stitch patterns [18,19], skin wrinkling [20] and multi-layered skin [21,22]. These factors can potentially make the skin flap simulation more accurate in general and have an impact on the preferred flap type for each patient.

3. Methods

In our pipeline, we first generate a 3D mesh from a 2D planar mesh of a specific flap design. Then we further process the intermediate 3D mesh to include multiple layers in the final 3D mesh. Next we run FEM simulations on the 3D mesh to get a deformed mesh after the simulation stabilizes. Given a 3D head model of a patient, this simulation can also be mapped to the patient's scan to help surgeons better visualize the flap design. An overview of our pipeline is shown in Fig. 1 and a list of software packages used at each stage is shown in Table 1.

3.1. 2D mesh creation

To start off, we construct a 2D planar skin patch with a known lesion location and size. The patch is currently designed to be circular in shape so that it is symmetrical around the center and it is easier to further extend to 3D in the next phase. The boundary of the skin patch is fixed. The skin flap is designed to be proportional to the lesion (an example can be seen in Fig. 2a–b). After the flap is designed, we create a triangulated mesh by specifying the mesh resolution and cut-out regions (see Fig. 2c). We used the publicly available library Triangle [23,24] to generate the triangulation.

To achieve cutting in certain flap types (such as rotation and advancement flaps), vertices along the cutting lines (e.g. the tail segments of the rhomboid flap) are duplicated and then we perform re-meshing to make the appropriate connections.

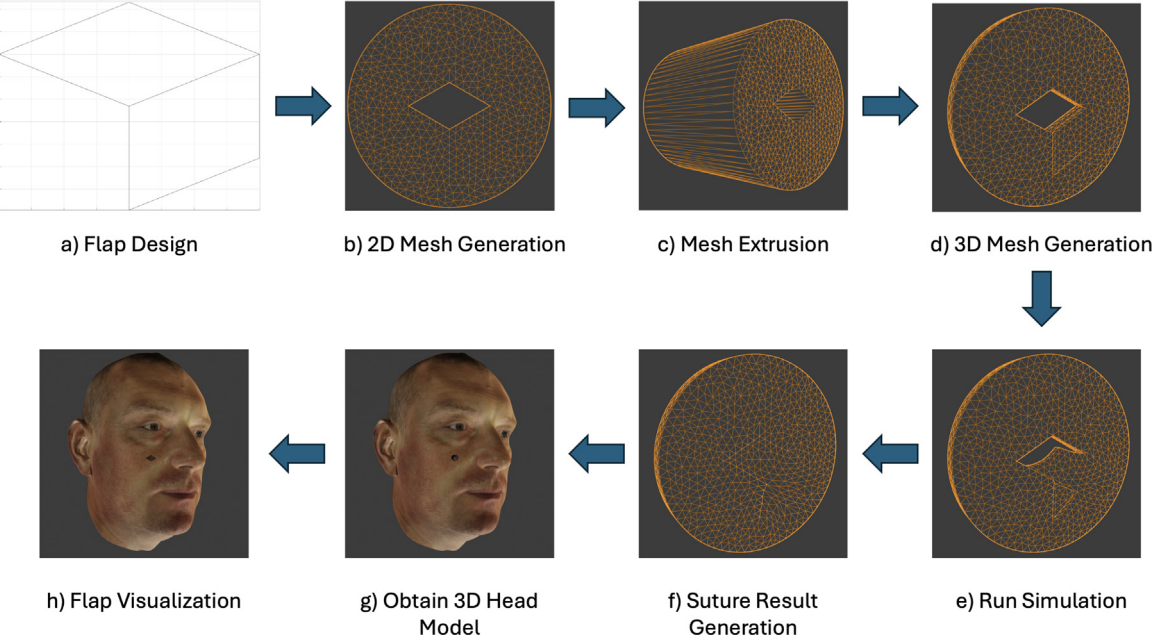


Fig. 1. Overview of pipeline, from mesh generation to visualization (face model was taken from [30] and lesion image was taken from Diepgen et al. [31]).

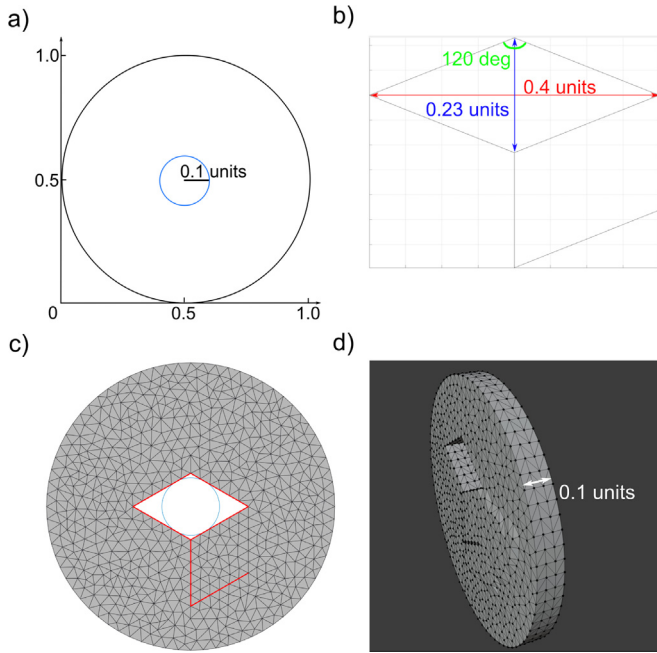


Fig. 2. Example 2D patch generation (lesion is shown in blue, fixed boundary is shown in black, and flap design is shown in red). (a) Lesion and fixed boundary; (b) Rhomboid flap design; (c) Rhomboid flap after triangulation; (d) Rhomboid flap side view.

3.1.1. Patch design for rhomboid flaps

For the case of rhomboid flap, we used a similar setup as in [2] where we normalized the patch to have a radius of 0.5 unit with its center located at (0.5, 0.5, 0) and a thickness of 0.1 unit. The lesion is assumed to be located inside a circular region with a radius of 0.1 as seen in Fig. 2a. Similar to [2], we performed our experiments on the most commonly used rhomboid flap type, the Limberg flap. The Limberg flap has equal edge lengths and a top angle of 120° [32] (see Fig. 2b for more detailed dimensions used in our experiments).

3.2. 3D mesh creation

After 2D mesh is created, the 3D mesh can be constructed using the 2D triangular mesh as a basis. The 2D mesh is first extruded using the linear extrusion filter in Paraview [25]. The extrusion generates an additional layer of vertices along with edges connecting the two layers along the boundary of the mesh. The 3D mesh was then imported into Blender [26] for further processing and for creating the undermining layer. The duplicated vertices along the cut line were first separated by a small gap to avoid tetrahedral generation issues. We then identified vertices for undermining. The vertices were selected from the underside of the single layer and were translated upwards by a small increment. The area of undermining is discussed in Section 3.3. More layers of the mesh were generated using the “mirror” modifier in Blender [26], with vertices that were close to each other being merged. For consistency, the undermined layer has the same thickness as the other layers. Finally, the tetrahedra within the 3D surface mesh were generated using GMsh’s built-in 3D method [27]. A sample mesh can be found at <https://www.kaggle.com/datasets/medcvr/rhomboid-skin-flap-simulations>.

3.3. Undermining

For any flap that involves advancing or rotating of the skin tissue, it is typical to perform the undermining procedure to give the skin more laxity. During an undermining procedure, the top layer of the skin is detached from the subcutaneous tissue. To simulate this procedure, we delete the connections between the undermined layer (e.g. the topmost layer) and the rest of the meshes. We experimented with undermining at different depth: thin layer undermining (undermine only the first layer while keep the bottom two layers attached) and thick layer undermining (undermine the top two layers from the bottom layer). We designed two systematic ways of calculating the undermining area: vertices expansion and boundaries based on center angle.

3.3.1. Vertices expansion

During the vertices expansion, we define the base case as the region of skin where we would like to rotate or advance during the procedure (see Fig. 3a as an example for rhomboid flap). Then to increase the

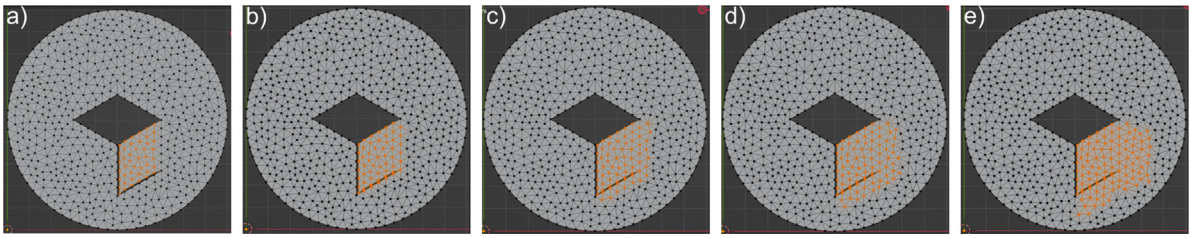


Fig. 3. Example undermining regions based on vertices expansion. (a) Case 1: Base case; (b) Case 2: Undermining region after 1 expansion; (c) Case 3: Undermining region after 2 expansions; (d) Case 4: Undermining region after 3 expansions; (e) Case 5: Undermining region after 4 expansions.

undermining area, we expand the base undermining region by n vertices each time, where n can be adjusted based on the mesh resolution (Fig. 3b to e shows examples of performing expansion when n is set to 1). A buffer region is also set so the undermined region does not get too close to the fixed boundary.

3.3.2. Boundaries based on center angle

Instead of vertices expansion, another method for setting the undermining region is to define the region with two bounds. The two boundaries of the undermining region can be defined with the following:

$$-m * (x - x_c) + (y - y_c) = 0, \quad (1)$$

where m is the slope of a line and it controls the direction of the boundary and x_c and y_c are the center of the patch (which is 0.5 for our case). For rhomboid flap, we fix one of the boundary by setting $m_1 = -0.1$ and increase the undermining area by changing m_2 for the second boundary. Each undermining area can be distinguished by the angle (center angle) between the two boundaries calculated as (based on basic trigonometry properties of finding the angle between two lines):

$$\theta = \arctan(\text{abs}((m_2 - m_1)/(1 + m_1 * m_2))), \quad (2)$$

where m_1 and m_2 are the slope parameters for the reference boundary and the second boundary, respectively (an example can be seen in Fig. 4a). The center angle defines how much we would like to span clock-wisely from the reference direction. Additional constraints can be added such as distance to the center of the patch and buffer distance to the outer boundary. Sample undermined regions for various center angles (θ) can be in Fig. 4.

3.4. The skin model and physical dimensions of the patch

The skin was simulated with a Neo-Hookean model with Young's modulus of 200 kPa, Poisson ratio of 0.48 and density of 1000 kg m⁻³ [33]. The radius of the basic skin patch was 5 cm, with the radius of the lesion area being 1 cm. The diagonals of the rhombus cut are 4 cm and 2.3 cm. The depth of the cut was 1 cm. The skin had three layers, each being 0.33 cm. Hence the thin undermining layer was 0.33 cm thick, and the thick undermining layer was 0.66 cm thick.

3.5. Suturing

After the mesh is generated, corresponding suture vertex pairs are automatically calculated by doing a search around each edge of the cutting line (the depth value is also taken into account to ensure vertices are sutured only to other vertices with the same initial depth). The suture process was implemented by adding zero rest-length springs between vertices to be sutured together. During the suturing process, the stiffness of the spring gradually increases until average distance between the two corresponding suture points is below a threshold, causing the corresponding suture vertices to move towards each other. After the simulation reaches steady state, the suture force can also be calculated and analyzed. Different stages of a rhomboid flap procedure are shown in Fig. 5.

3.6. Visualization through 3D head model mapping

During the simulation, the mesh vertices are saved after each iteration. Those saved vertices can be replayed in a sequence as an animation for a 3D head scan of a patient. To do this, we first obtain a 3D scan of a patient. Then we define a region of interest around the lesion area and this is the region represented by our simulation. Next, we cut out the mesh elements around the region of interest in the patient mesh and map our simulated mesh to the same region. To avoid gaps in the final output, the cut-out region in the patient mesh is slightly smaller than the simulation mesh. During the mapping process, the depth component of each mesh element is mapped to its closest neighbor in the patient mesh so that we can create curvatures similar to the original face mesh. Using the same principle, textures can also be copied to the simulated mesh to help surgeons visualize skin deformation after the procedure. A sample visualization is shown in Fig. 6.

4. Experiments

The skin flap FEM simulation was built based on the open-source library Bartels [29]. The multi-layer mesh allowed us to perform an investigation on the effect of the undermining area on the suturing force. The simulation iterated until convergence or a maximum number of 40 iterations. Newton's method was used to estimate the current velocity of vertices. The number of Newton iterations was set to be 20. Mesh vertex positions were then estimated based on the current velocity and time step. Running the simulation on a Mac Studio (Apple Inc.), a complete basic simulation for one case took 4-5 h.

4.1. Varying undermining area

This experiment was conducted on all 13 cases of undermining regions specified in Section 3.3. We also conducted the experiment on a patch with thick undermining layer. Upon investigating the final deformation of the mesh with the largest undermining area, we find that on the right bottom part of mesh, the boundary of movement is very close to the boundary of undermining. We shifted the mesh by 0.8 cm to the left and 1.5 cm upwards to align with the left undermining border and repeated the experiment. The shifted mesh is shown in Fig. 7b. Finally, we increased the size of the patch to increase the overall distance between the cut and the border (Fig. 7c).

4.2. Mesh setup

There are 46 vertices along the suture line and hence 23 pairs of vertices to suture. We indexed the vertices as shown in Fig. 8. A more detailed view of the mesh is shown in Figs. 9 and 10.

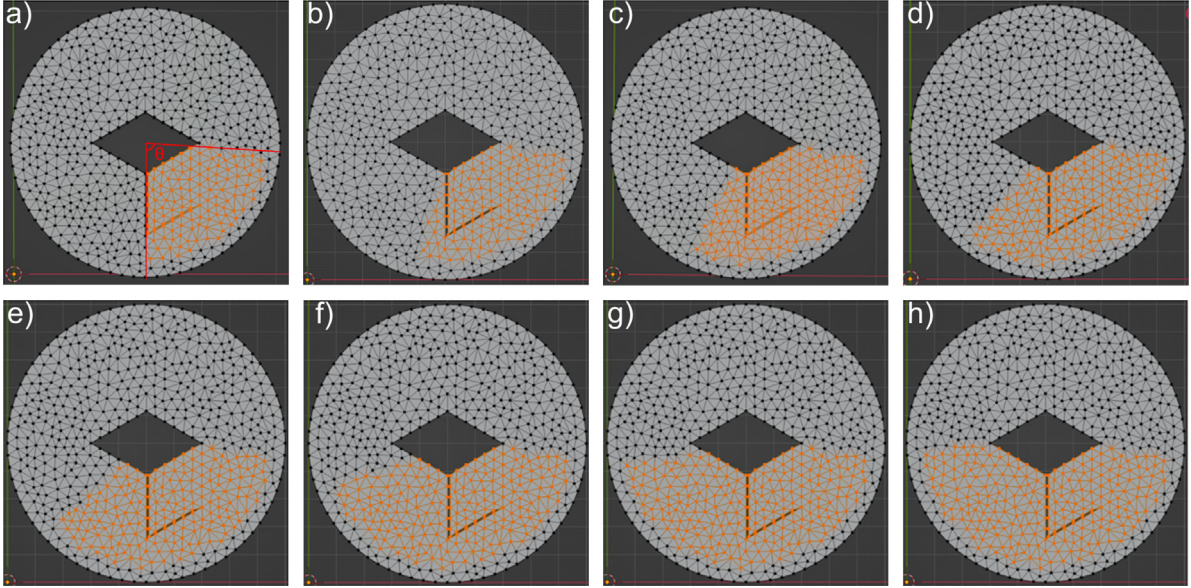


Fig. 4. Example undermining regions with boundaries based on center angle. (a) Case 6: angle = 84°; (b) Case 7: angle = 98°; (c) Case 8: angle = 111°; (d) Case 9: angle = 123°; (e) Case 10: angle = 132°; (f) Case 11: angle = 152°; (g) Case 12: angle = 163°; (h) Case 13: angle = 171°.

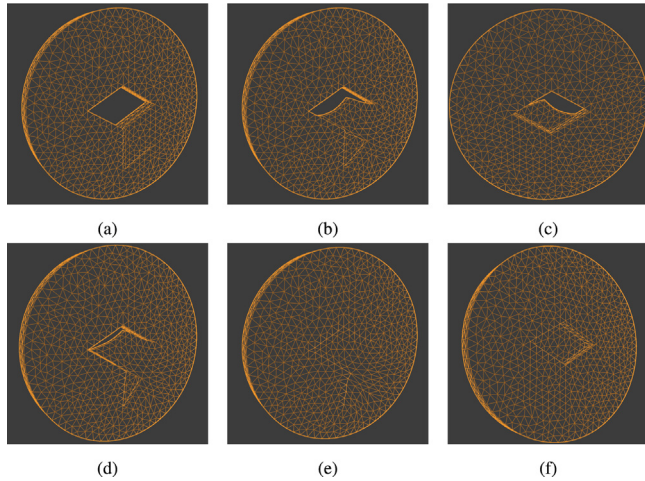


Fig. 5. Suturing process from beginning to end. In Fig. 5(b), it can be seen that the skin flap is undermined. (a) Initial design (iteration 0); (b) Iteration 20; (c) Back side of the mesh during iteration 20; (d) Iteration 25; (e) End of simulation (iteration 59); (f) Back side of the mesh during iteration 59.

5. Results

5.1. Thin layer of undermining

We take the average of the final three iterations of the simulation where the mesh has stabilized as the final suture force to analyze. In Fig. 11a and b, we plot the final suture force against vertex pair index.

The final suture force generally decreases as the undermining area increases. According to Fig. 11a and b, the force on the top vertices are generally smaller, which align with our expectation, since the top vertices can follow the same x/y movement of the bottom vertices. Therefore, we will mainly analyze the plot for the bottom vertices. From the plots, we can see that the undermining area mostly affects the force on vertex pairs 1 to 7, which is the vertical cut line in the undeformed mesh. The force remains more or less the same for vertex pairs 8 and onwards. From Fig. 11a, small undermining area (case 1 and 2) causes the forces go off the charts. The maximum suture force

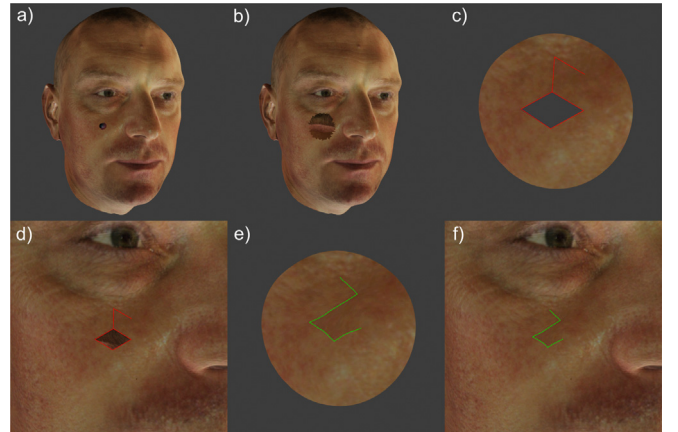


Fig. 6. Visualization on patient model. (a) 3D scan of a patient (face model was taken from [30] and lesion image was taken from Diepgen et al. [31].); (b) Cut out a hole around the lesion region; (c) Initial patch after texture mapping; (d) Map initial design to patient model; (e) Patch after simulation; (f) Map final simulation result to patient model.

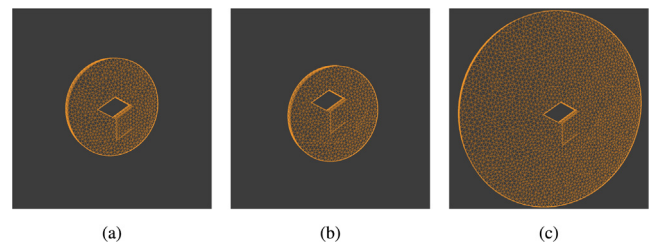


Fig. 7. Mesh setup of different experiments: (a) Basic mesh; (b) Shifted mesh; (c) Large mesh.

occurs at vertex pair 6, which is at the intersection of the vertical cut line and the rhombus.

In addition, case 3–6 are a group of undermining regions that have similar force profiles, and case 8 and onwards are another group of

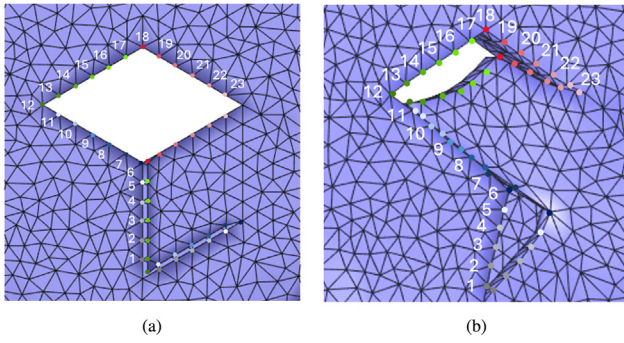


Fig. 8. Indexing pairing of the vertices from 1 to 23 for a rhomboid flap.

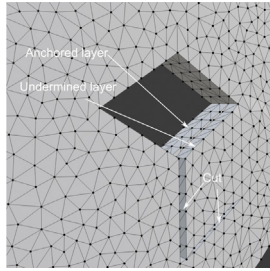


Fig. 9. A detailed view of the mesh with different layers.

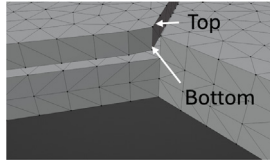


Fig. 10. The top vertices refer to the vertices on top of the undermining layer, and similarly for the bottom layer.

undermining regions that have similar force profiles. This indicates that the vertices that are included in case 3 but not in case 2 are significant, and vertices that are included in case 6 but not case 7 are significant. This also matches our expectations because referring to Figs. 3 and 4, these vertices are the ones that “cross” the cut line.

Besides, we observe that the force distribution for case 7 is not very consistent. Its force profile is not similar to case 6 and case 8, and also different in a thin undermining layer and a thick undermining layer case as shown in Section 5.2.

In Fig. 12, we overlay the final suture lines for all 13 cases. We also calculated the normalized Hausdorff distance (nHD) by taking case 5 as reference. The Hausdorff distance is normalized by the height of the bounding box of the suture line in case 5 (see Table 2).

According to Fig. 12, the suture line becomes more vertical from case 1 to case 5. Then it becomes more slanted from case 5 to case 13. This is reasonable because in the first case, the vertices along both the vertical and the slant line section in the undeformed mesh were not undermined so they did not have much freedom to move. This caused the suture line to be very slanted as the vertices moved to their mean position. However, as the undermining area increased and started to include the vertices that cross the slant line, vertices along and below the slant line moved more than the vertices along the vertical line, which were still not undermined in those cases. Therefore, the suture line became more vertical. From case 5 onwards, the mesh deformed more as the undermining area increased. From Fig. 12, we can again see

Table 2

nHD values of different cases in Fig. 12 (taking case 5 as reference); for the 2D case, $nHD = 0.086$.

Case	1	2	3	4	6	7
nHD	0.099	0.023	0.023	0.011	0.016	0.029
Case	8	9	10	11	12	13
nHD	0.062	0.062	0.068	0.066	0.079	0.088

that cases 2–6 have similar suture line shape, and cases 8 and onwards have another force profile.

In Fig. 12, we can also see how suture lines of different undermining areas compare with a 2D planar mesh with the same setup. It has a relatively large nHD value, indicating its shape is very different from the rest of the cases. In general, the suture line shape is an important basis for surgical planning and it can be used as a clue to determine the most optimal skin flap design.

5.2. Thick layer of undermining

We performed the same experiment but with a thicker undermining layer. We sutured the bottom, middle and top layer of vertices but here we only present the results on the bottom vertices and the top vertices. The results are shown in Fig. 11c and d.

The general trends are same as before. However, it can be seen in Fig. 11d that the thick undermining layer attenuates the forces on all the vertices on the top layer. This is predicted because the due to the increased thickness, the top vertices are even further away from the fixed vertices at the bottom. For the bottom vertices in Fig. 11c, for cases 3–6, the thick undermining layer accentuates the force on each vertex generally. For cases 8 and onwards, there is a smaller final suture force at vertex pair 6, but the suture force is amplified on other vertices. Additionally, the maximum force is no longer at vertex 6. We think that this might be due to the size of the mesh, and we performed additional experiments on modified meshes in Sections 5.3 and 5.5.

5.3. Shifted thin layer of undermining

We conducted experiments on the shifted mesh discussed in Section 4.1. We performed the 13 undermining cases shown in Figs. 3 and 4 and compare the final suture force on the bottom layer in each case with the basic version of the mesh in Fig. 13. Since the mesh is shifted mainly to investigate if there is more potential movement on the left bottom side of the mesh, we analyze the forces on vertex pairs 1–7.

The results match our predictions. In the shifted mesh, since there is more space on the right bottom part of the patch, but less space on the left bottom part of the patch, therefore, for the first 6 cases where the vertices on the left of the vertical cut line were not undermined, the force should be higher when there is even less space to move. This is shown in the first six plots of Fig. 13, where in the shifted mesh, the first 7 vertex pairs have larger force than in the basic mesh. For cases 8 onwards, the first 7 vertex pairs have smaller force than in the basic mesh. This is because now there are more space to move on the bottom of the mesh. Based on this difference, we experimented with a large patch so that the vertices have more freedom to move on either side of the vertical cut.

5.4. Shifted thick layer of undermining

We also tested the shifted mesh when the undermining layer is thick. The results are shown in Fig. 14.

The trends and results are similar to that discussed in Section 5.2 in that it amplifies the forces. In case 9 and 10, we also see that the force distribution is developing irregularly and the shifting of the maximum as we saw before.

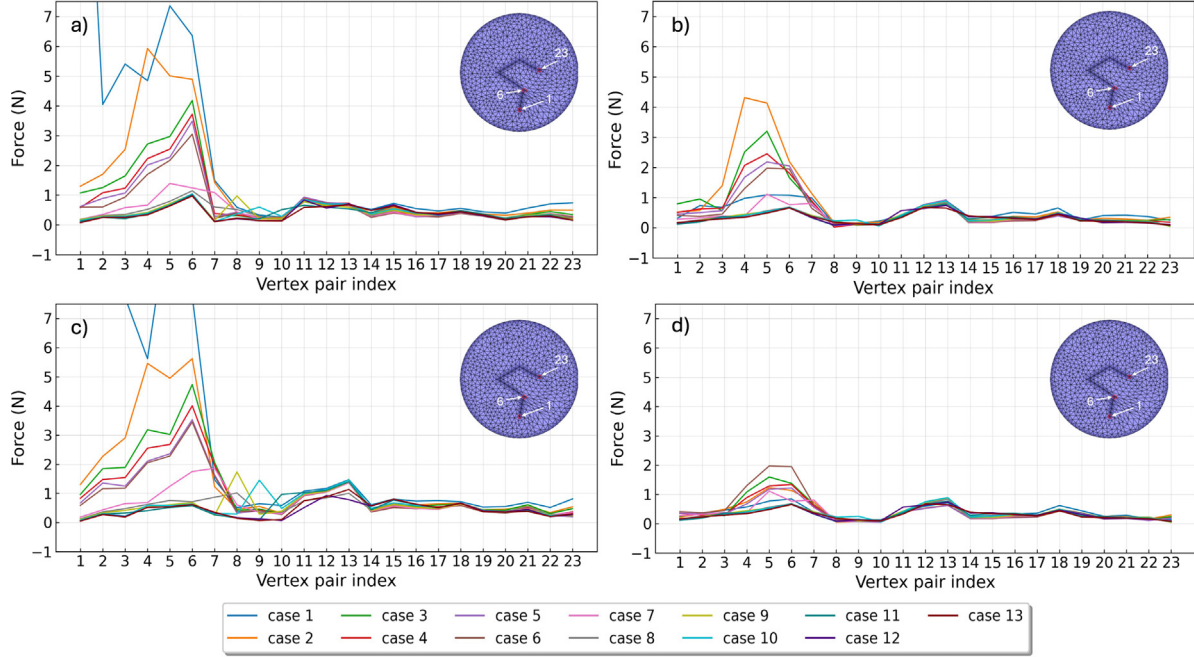


Fig. 11. Final suture force comparisons for different undermining cases shown in Figs. 3 and 4. The x-axis represents the suture index shown in Fig. 8 and the y-axis represents suture forces. (a) Bottom vertices of a thin undermining layer; (b) Top vertices of a thin undermining layer; (c) Bottom vertices of a thick undermining layer; (d) Top vertices of a thick undermining layer.

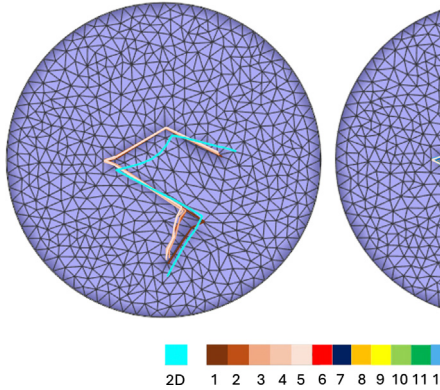


Fig. 12. Final suture line on 13 cases shown in Figs. 3 and 4. Left: cases 1 to 5; Right: cases 5 to 13; the cyan colored line represents suture line with a 2D planar mesh.

5.5. Large patch with thin undermining layer

We investigated the suture force on the large patch. Using the same undermining area, the large patch has approximately 3.7 times the number of vertices compared to the basic mesh. The simulation took 3–4 h for one iteration and around 5 days to complete. We only investigated the force in the case with largest undermining area. The comparison between the basic mesh and the large one is shown in Fig. 15.

Although for the top vertices in Fig. 15b, the results followed our prediction that generally the force should be smaller for all vertices, the results for the bottom vertices are very similar to that of the basic mesh. We believe that the large patch might be useful to a small extent given the similarity of the results with the basic mesh. Although theoretically the larger mesh could have more accurate results, the time trade-off is huge.

6. Visualizations on patient images

In addition to visualizing the simulation result on a head model, the saved mesh after each iteration can be used to create visualizations as an overlay on a patient' image as well (an overview is shown in Fig. 16). Upon getting an image of the patient, the lesion and the surrounding area will be identified. After the simulation finishes, each iteration will be texture mapped based on the identified region in the patient image (including the initial and final mesh as shown in Fig. 16). Then based on landmarks detected from a face tracker similar to [35], each of the texture mapped patch can be mapped back to the patient's face as a animation sequence to show the different stages of the skin flap procedure. Comparing to Guo et al. [35], this pipeline produces more realistic visualization as it includes tissue and suture line deformation.

7. Conclusion

We explored the effect of different undermining areas of the rhomboid skin flap on the suture force along the suture line using a 3D mesh. We included an undermining layer with different depth with a thin versus a thick undermining layer. To increase the accuracy of the simulation and ensure that the fixed boundary of the skin patch is located far from the incision, we also tried using a mesh where the incision is shifted. The results match our prediction that the larger the undermining area, the smaller the maximum force along the suture line. In the cases we have tested, cases 11–13 have the lowest forces among all cases and also have similar force profile. Since case 11 requires the least undermining in these 3 cases, we can conclude that the undermining region in case 11 is optimal. We also find that the vertices along the vertical and slant incision of the rhomboid flap play more significant roles in the final force comparison. The indices near the closure of the donor site (around index 6) have the largest suture force, which agrees with the findings by Larrabee et al. [36]. Varying

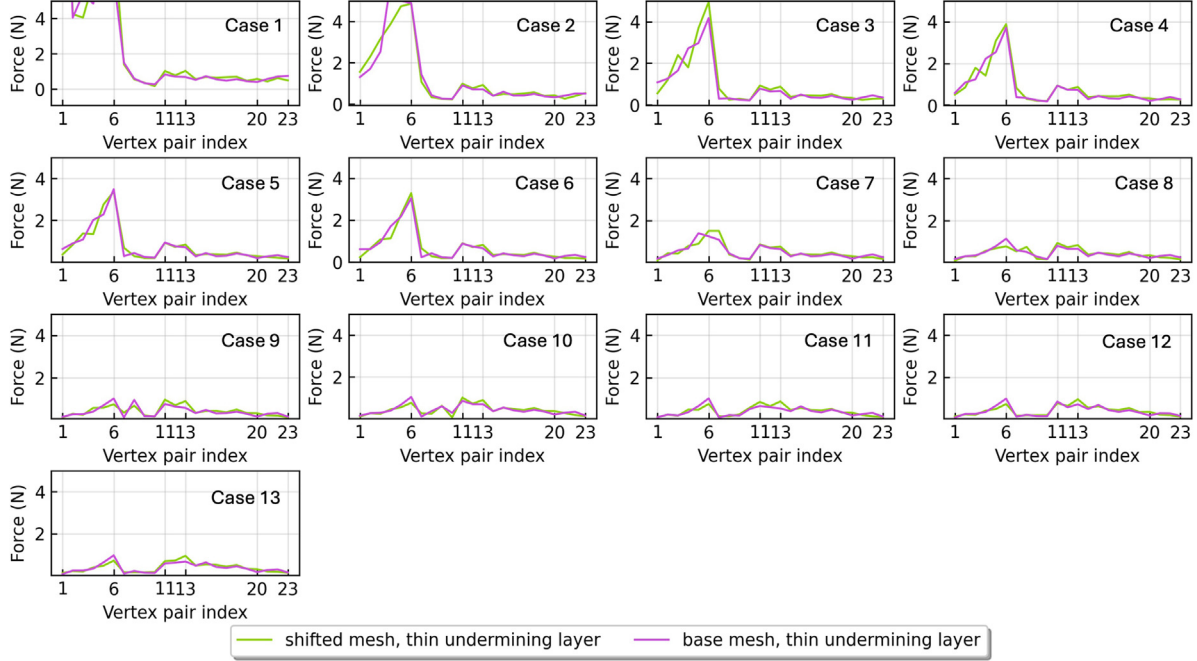


Fig. 13. Final suture force comparisons for a thin undermining layer in shifted mesh versus non-shifted mesh. Each graph represents an undermining case shown in Figs. 3 and 4.

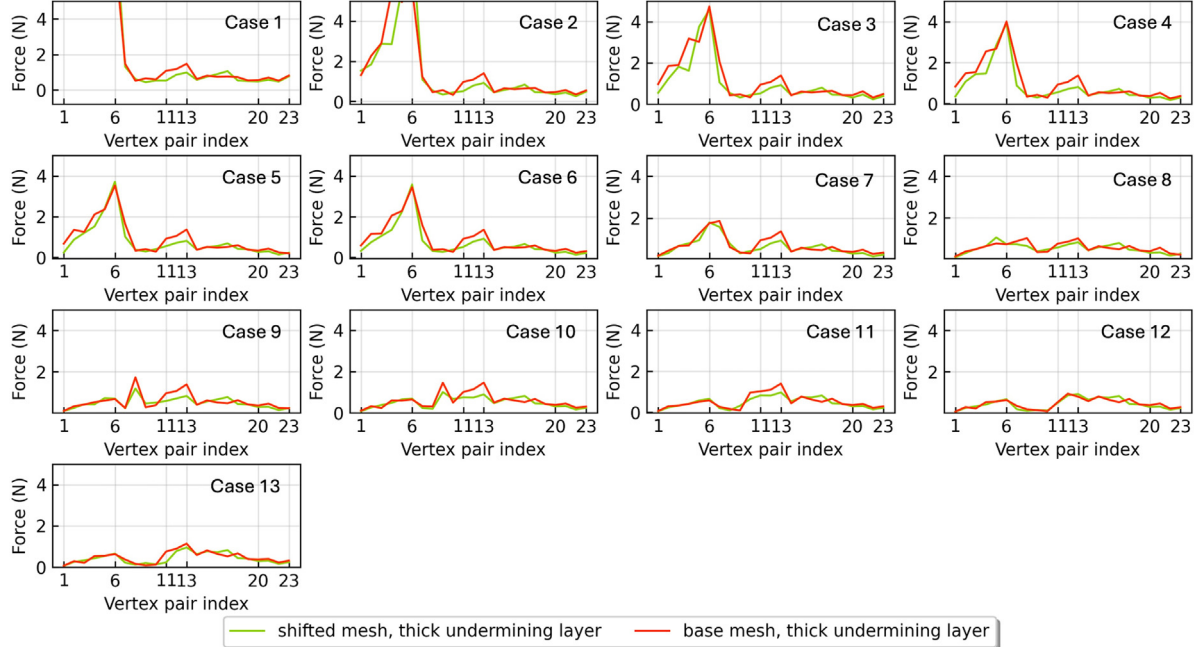


Fig. 14. Final suture force comparisons for a thick undermining layer in shifted mesh versus non-shifted mesh. Each graph represents an undermining case shown in Figs. 3 and 4.

undermining areas cause the final suture line to be different (especially along the tail region), which can be an important clue for deciding the most optimal skin flap design.

Although a variety of software designs have enabled surgeons to better plan out their local resections and reconstructions, a common challenge is providing objective data to guide the decision-making process. For example, following excision of a cutaneous lesion in the face, surgeons will often use their prior experience, comfort with reconstructive options and training to guide their decisions in local flap

selection. However, a variety of factors may limit the optimal choice selected. One of these factors is tissue undermining. Depending on the surrounding anatomy, and structures for which boundaries cannot be crossed (i.e. nasal subunits, the eye, nasolabial fold, etc.), the proximity to these structures may limit the amount of tissue undermining that is possible. Therefore, determining the ideal amount of undermining to minimize tension of closure along RSTLs, while also limiting the deformation of surrounding anatomic subunits, is critical to the entire flap design process. Our study provides objective data to assist surgeons

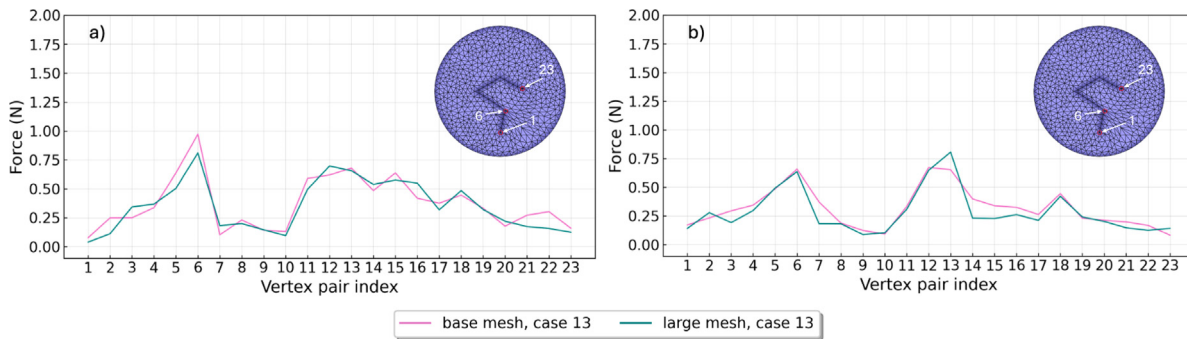


Fig. 15. Final suture force comparisons for the largest undermining area (case 13) shown in Fig. 4 for a large patch. (a) Bottom vertices of a thin undermining layer; (b) Top vertices of a thin undermining layer.

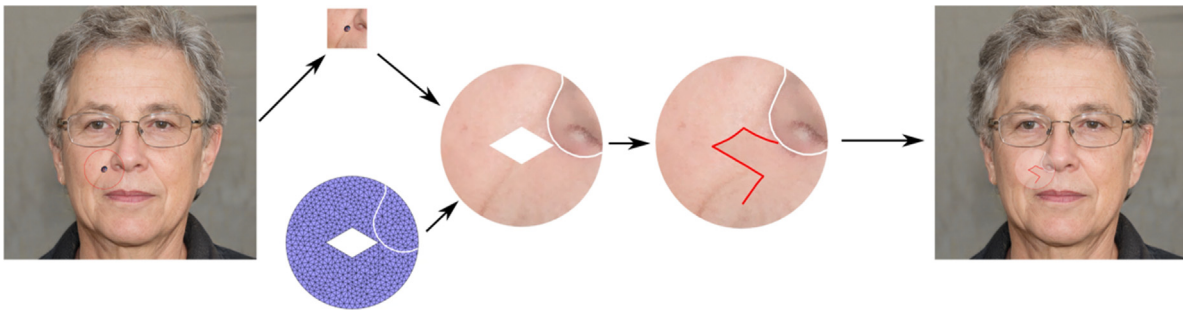


Fig. 16. Sample visualization workflow for mapping rendered patch onto a patient's face image. Sample face image without any overlay and lesion was generated with StyleGAN2 [34].

Source: Lesion image was taken from Diepgen et al. [31].

in the flap design process with one of the most challenging local flap reconstructions to plan, the rhomboid flap.

However, in our investigation, we have used uniform elasticity mesh, which does not completely represent real life scenarios. A possible extension would be to use different elasticity for different layers of skin in the mesh. It would also be beneficial to investigate the orientation of the rhomboid flap with respect to RSTLs using the 3D mesh with undermining, similar to work done previously [2]. Lastly, we could also repeat the same experiments by further enlarging the undermining region similar to Larrabee et al. [36] and making the undermining region asymmetric [37]. From a clinical perspective, future directions include obtaining feedback from the clinical end-users and ultimately aim towards implementation of this software into clinical practice where it can be used in patient/learner education and perhaps as a means of minimizing morbidity where objective data can assist in either opting in or out of a particular flap design.

CRediT authorship contribution statement

Wenzhangzhi Guo: Writing – original draft, Supervision, Software, Methodology, Investigation, Conceptualization. **Allison Tsz Kwan Lau:** Writing – original draft, Visualization, Software, Investigation, Data curation. **Joel C. Davies:** Writing – review & editing, Supervision, Conceptualization. **Vito Forte:** Writing – review & editing, Supervision, Conceptualization. **Eitan Grinspun:** Writing – review & editing, Supervision, Methodology. **Lueder Alexander Kahrs:** Writing – review & editing, Supervision, Project administration, Methodology, Funding acquisition, Conceptualization.

Declaration of competing interest

The authors declare that they have no known competing financial interests or personal relationships that could have appeared to influence the work reported in this paper.

Data availability

Data will be made available on request.

Acknowledgments

We would like to thank Ruiting Chen and Ava Oveis for their contributions to the project. WG would like to thank the support from NSERC Alexander Graham Bell Canada Graduate Scholarship-Doctoral (CGS D).

Appendix A. Supplementary data

Supplementary material related to this article can be found online at <https://doi.org/10.1016/j.cag.2024.104057>.

References

- [1] Baker S. Local flaps in facial reconstruction. 2nd ed.. Mosby; 2007.
- [2] Guo W, Trusty T, Davies JC, Forte V, Grinspun E, Kahrs LA. Analysis of suture force simulations for optimal orientation of rhomboid skin flaps. In: Greenspan H, Madabhushi A, Mousavi P, Salcudean S, Duncan J, Syeda-Mahmood T, Taylor R, editors. Medical image computing and computer assisted intervention – MICCAI 2023. Cham: Springer Nature Switzerland; 2023. p. 576–86. http://dx.doi.org/10.1007/978-3-031-43996-4_55.
- [3] Zhang J, Zhong Y, Gu C. Deformable models for surgical simulation: A survey. IEEE Rev Biomed Eng 2018;11:143–64. <http://dx.doi.org/10.1109/RBME.2017.2773521>.
- [4] Golden JM. The problem of a moving rigid punch on an unlubricated visco elastic half-plane. Quart J Mech Appl Math 1979;32(1):25–52. <http://dx.doi.org/10.1093/qjmam/32.1.25>.
- [5] Machiraju C, Phan A-V, Pearsall AW, Madanagopal S. Viscoelastic studies of human subscapularis tendon: Relaxation test and a Wiechert model. Comput Methods Programs Biomed 2006;83(1):29–33. <http://dx.doi.org/10.1016/j.cmpb.2006.05.004>.
- [6] Wang X, Schoen JA, Rentschler ME. A quantitative comparison of soft tissue compressive viscoelastic model accuracy. J Mech Behav Biomed Mater 2013;20:126–36. <http://dx.doi.org/10.1016/j.jmbbm.2013.01.007>.

- [7] Irving G, Schroeder C, Fedkiw R. Volume conserving finite element simulations of deformable models. *ACM Trans Graph* 2007;26(3):13–es. <http://dx.doi.org/10.1145/1276377.1276394>.
- [8] Sheen SH, Larionov E, Pai DK. Volume preserving simulation of soft tissue with skin. *Proc ACM Comput Graph Interact Technol* 2021;4(3). <http://dx.doi.org/10.1145/3480143>.
- [9] Pereira K, Ringel M, Miga MI. Image reconstruction and tissue separation modeling with XFEM for surgical visualization and guidance. In: Siewerdsen JH, Rettmann ME, editors. Medical imaging 2024: image-guided procedures, robotic interventions, and modeling. Vol. 12928, SPIE, International Society for Optics and Photonics; 2024, p. 129281F. <http://dx.doi.org/10.1117/12.3008635>.
- [10] Wang Q, Tao Y, Cutting C, Sifakis E. A computer based facial flaps simulator using projective dynamics. *Comput Methods Programs Biomed* 2022;218:106730. <http://dx.doi.org/10.1016/j.cmpb.2022.106730>.
- [11] Mitchell N, Cutting C, Sifakis E. GRIDiron: An interactive authoring and cognitive training foundation for reconstructive plastic surgery procedures. *ACM Trans Graph* 2015;34(4). <http://dx.doi.org/10.1145/2766918>.
- [12] Retel V, Vescovo P, Jacquet E, Trivaudey F, Varchon D, Burtheret A. Nonlinear model of skin mechanical behaviour analysis with finite element method. *Skin Res Technol* 2001;7(3):152–8. <http://dx.doi.org/10.1034/j.1600-0846.2001.70302.x>.
- [13] Pauchot J, Remache D, Chambert J, Elkhyat A, Jacquet E. Finite element analysis to determine stress fields at the apex of V-Y flaps. *Eur J Plast Surg* 2013;36(3):185–90. <http://dx.doi.org/10.1007/s00238-012-0776-1>.
- [14] Yang Z-L, Peng Y-H, Yang C, Cheng B, Ji M-K, Zhao Y. Preoperative evaluation of V-Y flap design based on computer-aided analysis. *Comput Math Methods Med* 2020;2020:8723571. <http://dx.doi.org/10.1155/2020/8723571>.
- [15] Capek L, Jacquet E, Dzan L, Simunek A. The analysis of forces needed for the suturing of elliptical skin wounds. *Med Biol Eng Comput* 2012;50(2):193–8. <http://dx.doi.org/10.1007/s11517-011-0857-5>.
- [16] Rajabi A, Dolovich AT, Johnston J. From the rhombic transposition flap toward Z-plasty: An optimized design using the finite element method. *J Biomech* 2015;48(13):3672–8. <http://dx.doi.org/10.1016/j.jbiomech.2015.08.021>.
- [17] Remache D, Chambert J, Pauchot J, Jacquet E. Numerical analysis of the V-Y shaped advancement flap. *Med Eng Phys* 2015;37(10):987–94. <http://dx.doi.org/10.1016/j.medengphy.2015.08.005>.
- [18] Chanda A, Unnikrishnan V. A realistic 3d computational model of the closure of skin wound with interrupted sutures. *J Mech Med Biol* 2017;17(01):1750025. <http://dx.doi.org/10.1142/S0219519417500257>.
- [19] Lott-Crumpler D, Chaudhry H. Optimal patterns for suturing wounds of complex shapes to foster healing. *J Biomech* 2001;34(1):51–8. [http://dx.doi.org/10.1016/S0021-9290\(00\)00160-3](http://dx.doi.org/10.1016/S0021-9290(00)00160-3).
- [20] Cavicchi A, Gambarotta L, Massabò R. Computational modeling of reconstructive surgery: The effects of the natural tension on skin wrinkling. *Finite Elem Anal Des* 2009;45(8):519–29. <http://dx.doi.org/10.1016/j.finel.2009.02.006>.
- [21] Flynn CO, McCormack BA. A three-layer model of skin and its application in simulating wrinkling. *Comput Methods Biomed Eng* 2009;12(2):125–34. <http://dx.doi.org/10.1080/10255840802529933>.
- [22] Flynn C, McCormack BA. Simulating the wrinkling and aging of skin with a multi-layer finite element model. *J Biomech* 2010;43(3):442–8. <http://dx.doi.org/10.1016/j.jbiomech.2009.10.007>.
- [23] Shewchuk JR. Triangle: Engineering a 2D quality mesh generator and Delaunay triangulator. In: Lin MC, Manocha D, editors. Applied computational geometry towards geometric engineering. Berlin, Heidelberg: Springer Berlin Heidelberg; 1996, p. 203–22. <http://dx.doi.org/10.1007/BFb0014497>.
- [24] Jacobson A, et al. Gptoolbox: geometry processing toolbox. 2024, <http://github.com/alecjacobson/gptoolbox>.
- [25] Ahrens JP, Geveci B, Law CC. Paraview: An end-user tool for large-data visualization. In: The visualization handbook. 2005, p. 717–31. <http://dx.doi.org/10.1016/B978-012387582-2/50038-1>.
- [26] The Blender Foundation. Blender. 2024, <https://www.blender.org>.
- [27] Geuzaine C, Remacle J-F. Gmsh: A 3-D finite element mesh generator with built-in pre- and post-processing facilities. *Internat J Numer Methods Engrg* 2009;79(11):1309–31. <http://dx.doi.org/10.1002/nme.2579>.
- [28] The MathWorks Inc. MATLAB version: 9.13.0 (r2022b). 2022, <https://www.mathworks.com>.
- [29] Levin D, Winter A, Bang S. Bartels. 2024, <https://github.com/dilevin/Bartels>.
- [30] Artec3D. Face by Artec 3D. 2024, <https://www.artec3d.com/3d-models/face>.
- [31] Diepgen T, et al. GS. DermIS - dermatology online Atlas. 2022, <https://www.dermis.net/dermisroot/en/home/index.htm>.
- [32] Borges A. Choosing the correct Limberg flap. *Plast Reconstr Surg* 1978;62(4):542–5. <http://dx.doi.org/10.1097/00006534-197810000-00007>.
- [33] Li C, Guan G, Reif R, Huang Z, Wang RK. Determining elastic properties of skin by measuring surface waves from an impulse mechanical stimulus using phase-sensitive optical coherence tomography. *J R Soc Interface* 2012;9(70):831–41. <http://dx.doi.org/10.1098/rsif.2011.0583>.
- [34] Karras T, Laine S, Aittala M, Hellsten J, Lehtinen J, Aila T. Analyzing and improving the image quality of StyleGAN. In: Proc. CVPR. 2020.
- [35] Guo W, Forte V, Davies JC, Kahrs LA. An interactive augmented reality software for facial reconstructive surgeries. *Comput Methods Programs Biomed* 2024;244:107970. <http://dx.doi.org/10.1016/j.cmpb.2023.107970>.
- [36] Larrabee WF, Trachy R, Sutton D, Cox K. Rhomboid flap dynamics. *Arch Otolaryngol* 1981;107(12):755–7. <http://dx.doi.org/10.1001/archotol.1981.00790480031008>.
- [37] Topp SG, Lovald S, Khraishi T, Gaball CW. Biomechanics of the Rhombic Transposition Flap. *Otolaryngol Head Neck Surg* 2014;151(6):952–9. <http://dx.doi.org/10.1177/0194599814551128>.